

Emergent Wigner phases in moiré superlattice from deep learning

Xiang Li^{1*}, Yubing Qian^{1,4}, Weiluo Ren¹, Yang Xu^{2,3†}, and Ji Chen^{4,5‡}

¹ByteDance Research, Fangheng Fashion Center, No. 27, North 3rd Ring West Road, Haidian District, Beijing 100098, People's Republic of China

²Beijing National Laboratory for Condensed Matter Physics, Institute of Physics, Chinese Academy of Sciences, Beijing 100190, China

³School of Physical Sciences, University of Chinese Academy of Sciences, Beijing 10049, China

⁴School of Physics, Peking University, Beijing 100871, People's Republic of China.

⁵Interdisciplinary Institute of Light-Element Quantum Materials, Frontiers Science Center for Nano-Optoelectronics, Peking University, Beijing 100871, People's Republic of China

June 18, 2024

Abstract Moiré superlattice designed in stacked van der Waals material provides a dynamic platform for hosting exotic and emergent condensed matter phenomena. However, the relevance of strong correlation effects and the large size of moiré unit cells pose significant challenges for traditional computational techniques. To overcome these challenges, we develop an unsupervised deep learning approach to uncover electronic phases emerging from moiré systems based on variational optimization of neural network many-body wavefunction. Our approach has identified diverse quantum states, including novel phases such as generalized Wigner crystals, Wigner molecular crystals, and previously unreported Wigner covalent crystals. These discoveries provide insights into recent experimental studies and suggest new phases for future exploration. They also highlight the crucial role of spin polarization in determining Wigner phases. More importantly, our proposed deep learning approach is proven general and efficient, offering a powerful framework for studying moiré physics.

Main Moiré superlattices, spanning from twisted graphene [1–3], transition metal dichalcogenides (TMDs) [4–9], and other systems, have attracted significant research interest in condensed matter physics over the last few years [10]. They provide a flexible platform to tune the electronic, magnetic, and optical properties of materials, and explore strongly correlated and topological phenomena such as unconventional superconductivity [2, 11] and correlated insulating behaviors [2–9]. For example, recent discoveries of new quantum phases, including the generalized Wigner crystal [6–9], known for their unique symmetry and particle arrangements, have provided deep insights into the behaviors of strongly correlated systems. These insights have been further enriched recently by Wigner molecular crystals emerging from multi-hole artificial atoms in twisted WS₂ homobilayer [12, 13], underscoring the tunable feature of moiré superlattices.

Theoretically, a grand challenge remains that a general theoretical approach to handling strong electron correlation effects of moiré system is lacking, and the current investigations mostly rely on traditional computational methods, such as classic Monte Carlo [6] and Hartree-Fock approximation [12–14]. While these calculations may provide qualitative explanations for experimental results and make other predictions, it is questionable whether all essential correlated physics has been captured. The importance of electron correlation effects on the phase transitions in a moiré system is further highlighted with a combination of auxiliary field quantum Monte Carlo and diffusion Monte Carlo [15]. In recent years, powerful approaches based on deep learning architecture have been developed to treat quantum many-body problems. Based on the universality and expressiveness of neural networks, quantum many-body states can be well-represented without assuming a limited traditional *ansatz*, and new insights into

the correlation effects are revealed. However, so far these deep learning approaches can only be applied to simple lattice models [16], chemical molecules [17–19], uniform electron gases [20–22], small solids [20], and isolated Wigner molecules [23].

In this work, we develop a neural network based wavefunction methodology for moiré systems. The neural network wavefunction is trained via the variational quantum Monte Carlo method in an unsupervised manner. Focusing on the family of TMD materials over a wide range of particle fillings, we unveil a sequence of intriguing phases. At fractional fillings, symmetry preserved and broken Wigner crystal emerges with varying fillings. At integer fillings, electron correlations lead to a rich diagram of Wigner phases, including the recently observed Wigner molecular crystals, and Wigner covalent crystals discovered in this work. This study underscores the pivotal role of electron correlations captured by deep learning in unlocking and leveraging the quantum phenomena inherent in moiré superlattices.

Deep learning architecture Fig. 1 summarizes the overall workflow. First of all, to explore the quantum phases of moiré materials, a neural network is employed to represent the many-body wavefunction. The neural network wavefunction Ψ_{net} has the following form

$$\Psi_{\text{net}} = \det[e^{i\mathbf{k}_i \cdot \mathbf{r}_j} u_{\mathbf{k}_i}(\mathbf{r}_1, \dots, \mathbf{r}_N)]. \quad (1)$$

Compared with traditional wavefunction, Ψ_{net} explicitly includes the features of all particles ($\mathbf{r}_1, \dots, \mathbf{r}_N$) in the formulation, permitting it to capture all the correlations. Specifically, particle features \mathbf{r}_i are converted to be periodic and fed into permutation-equivalent neural networks [18, 20] to construct the generalized Bloch functions $u_{\mathbf{k}_i}(\mathbf{r}_1, \dots, \mathbf{r}_N)$ in Eq. (1), which together with the Slater determinant form a periodic, complex-valued, and anti-symmetric many-body wavefunction for superlattice. Millions of

* lixiang.62770689@bytedance.com

† yang.xu@iphy.ac.cn

‡ ji.chen@pku.edu.cn

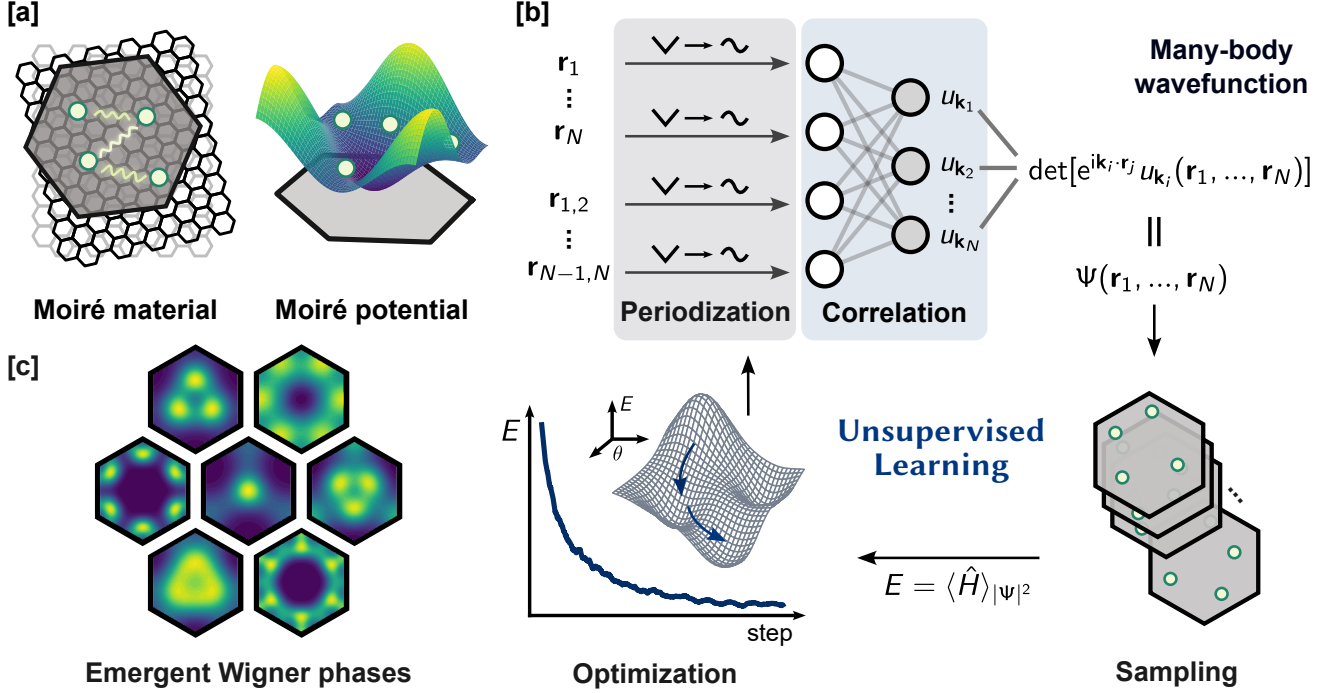


Fig. 1 | Workflow of deep learning approach. **a**, plotted structure of moiré materials, particles are constrained by moiré potential and interact with each other via Coulomb interaction. **b**, a sketch of deep learning approach. The upper part illustrates a neural network wavefunction for a moiré superlattice. Particle features \mathbf{r} are converted to be periodic and then fed into neural networks, forming the many-body wavefunction *ansatz* Ψ . The neural network is then trained using unsupervised learning. Specifically, variational Monte Carlo is applied to sample patterns and minimize the energy expectation $\langle \hat{H} \rangle_{|\Psi|^2}$. During the training iterations, the neural network wavefunction gradually approaches the ground state. **c**, emergent Wigner crystal phases in our simulation, including Mott insulator, Wigner molecular crystals, and other exotic phases.

parameters are embedded in the neural network, making it a powerful and convenient tool for expressing quantum states of distinct symmetries.

Given the neural network wavefunction and the Hamiltonian of a real material, one can employ the variational Monte Carlo (VMC) method to efficiently optimize the neural network parameters. VMC is based on the variational principle of quantum mechanics, which states the ground state has the lowest energy among all the solutions to the stationary Schrödinger equation. Therefore, the VMC training of the neural network is an unsupervised process, which further guarantees the reliability of our deep learning approach.

Moiré superlattice Moiré superlattice appears when two layers of van der Waals material overlap each other, with mismatched lattice constants and/or twisted angles. The superlattice formed features a significantly large lattice constant and contains thousands of atoms in the unit cell, which makes it unrealistic to employ the full *ab initio* Hamiltonian of a moiré material in the current workflow. Therefore, in this work we focus on the low-energy effective Hamiltonian of TMDs [4], which reads

$$\hat{H} = \sum_i \left[-\frac{\Delta_i}{2m^*} + V_M(\mathbf{r}_i) \right] + \frac{1}{2} \sum_{i \neq j} \frac{1}{\epsilon |\mathbf{r}_i - \mathbf{r}_j|},$$

$$V_M(\mathbf{r}) = -2V \sum_{i=1}^3 \cos(\mathbf{b}_i \cdot \mathbf{r} + \phi).$$

This model describes doping holes of TMD materials near Fermi surface and m^* refers to the effective mass of valence band edge. V_M is moiré potential experienced by holes across the whole moiré materials. \mathbf{b}_i denotes the reciprocal vector of moiré cell, and V, ϕ are parameters depending on the material. When moiré materials get twisted to critical angles, flat band appears and Coulomb interaction becomes dominant, which accounts for the last term in Eq. (2) with ϵ referring to effective dielectric constant. A uniform charge background is also necessary to make the whole system neutral and remove divergence in Coulomb interactions.

The effective Hamiltonian has included the key feature of Coulomb interactions and greatly simplifies the problem, so it has been successfully used in studies of TMD heterobilayers such as WSe_2/WS_2 and Γ -valley homobilayers such as twisted WS_2 [4, 24]. It is worth noting that electron correlations in such an effective Hamiltonian are as non-trivial as the *ab initio* Hamiltonian, and an exact solution remains extremely difficult. The most prevalent Hartree-Fock method treats particles independent from each other, which would lose the correlation effects. More accurate methods such as the full configuration interaction theory exist [25–27], but they are only applicable to isolated small molecules. Our deep learning wavefunction approach achieves an optimal balance of accuracy and efficiency, making it a very promising tool for studying moiré systems.

(2) **Generalized Wigner crystal** In 1934, Eugene Wigner imagined an electron-only crystal, where electrons spontaneously organize into special patterns as their density decreases. The pursuit

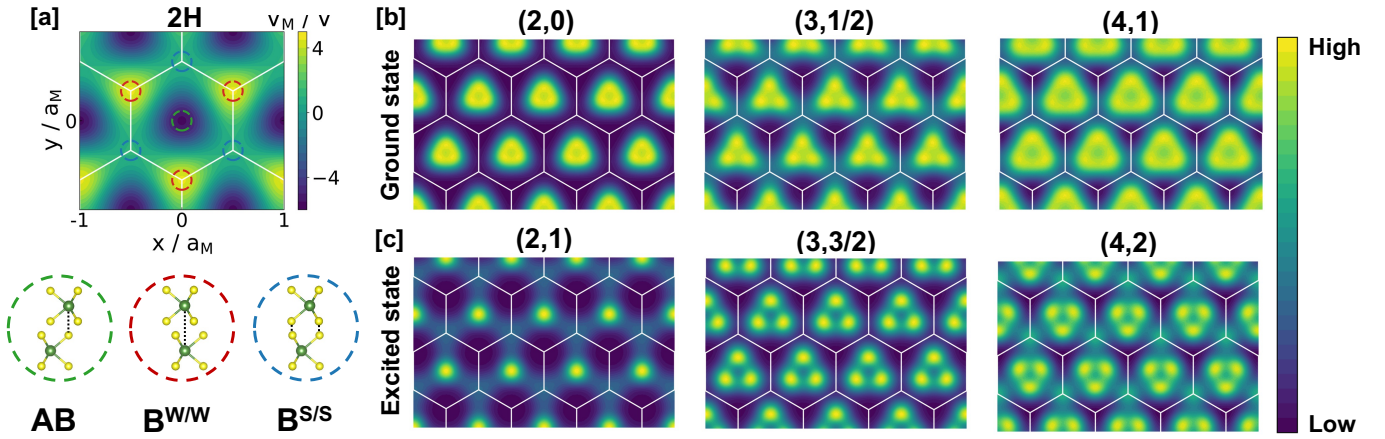


Fig. 2 | Calculated density pattern of 2H WS₂ homobilayer. Tuples above the figure denote the particle fillings and the magnetic number of spin (ν, S_z). **a**, moiré potential of 2H WS₂ homobilayer. a_M denotes length of moiré cell and is set to 9.8 nm. Colored circles denote regions with different stack patterns. **b-c**, calculated ground state and excited state of 2H WS₂ at different particle fillings ν and magnetic numbers S_z .

of Wigner crystals has continued ever since, and driven significant condensed matter physics discoveries for decades. Recently, the investigation is expanded to generalized Wigner crystals in moiré materials [6–8, 28]. We first employ our deep learning methods to reproduce the experimentally observed Wigner phases in a WSe₂/WS₂ heterobilayer at fractional particle fillings $\nu \leq 1$, which serves as a validation of our methodology. The results are presented in Supplementary Fig. 4. In line with recent experimental results [6–9], we observe a Mott insulator phase instead of metal at $\nu = 1$ manifesting the strong correlation characters of such systems. We also observe various Wigner crystal phases at $\nu = 1/3, 2/3$ with C_3 symmetry, and symmetry-breaking stripe phases at $\nu = 1/2, 2/5, 1/6$, which are also consistent with recent optical anisotropy and electronic compressibility measurements [28].

Wigner molecular crystal Beyond the aforementioned fractional filling, recent research has been extended to multiple integer fillings of moiré superlattice, wherein multiple particles are assigned to a single moiré cell [12, 13]. These particles aggregate and form a “molecule”, naturally residing at the minimum of the moiré potential. Upon the activation of Coulomb repulsion, these molecules slightly disperse and form the so-called Wigner molecular crystal [12]. These molecular crystals are recently observed in 2H WS₂ homobilayer via scanning tunneling microscopy (STM) [13], prompting us to employ our neural network to explain this observation.

Quantum states of 2H WS₂ with different fillings ν and spin quantum numbers S_z are investigated and the results are plotted in Fig. 2. At $\nu = 2$ fillings, we find $S_z = 0$ state has the lowest energy in which two spin-opposite holes are all placed in AB region. If we align their spins parallel, one hole will depart due to Pauli exclusion and transfer to the B^{S/S} region, forming a charge-transfer insulator as an excited state [29]. A more intricate situation happens at $\nu = 3$. The previous understanding of the experimental pattern at $\nu = 3$ presumes the ground state to be fully spin-polarized [13], while we find that the $S_z = 1/2$ state presents a rather similar trimer pattern with $S_z = 3/2$ and a slightly lower energy 0.4 meV / hole (Supplementary Fig. 2).

In either trimer pattern, particles mainly accumulate at the vertexes of the triangle, while the center remains empty to minimize Coulomb interactions. More detailed experimental characterization is desired to resolve such a delicate competition and confirm the true ground state. Concerning $\nu = 4, S_z = 1$ state is identified as the ground state, exhibiting a more hollow triangle pattern. It is also intriguing to see a flipping of the triangle when the system enters a fully polarized $S_z = 2$ state, which can be further verified in experiment by applying a magnetic field. Overall, the predicted ground-state patterns from deep learning are perfectly consistent with recent STM observations at different fillings [13], showing the reliability of our deep learning approach.

Predicting new phases Having demonstrated the capability of our deep learning approach to reproduce the experimentally observed phases, we now proceed to further explore new phases. As an example, we examine the WS₂ homobilayer with 3R configuration, which differs from 2H configuration due to the opposite orientations of layers [24]. Notably, the energies of different Bernal regions (B^{W/S} and B^{S/W}) coincide with each other in 3R WS₂, resulting in an underlying C_6 symmetry (see Fig. 3a).

The calculated ground states at different particle fillings are plotted in Fig. 3b. The first interesting phenomenon we observe is the spontaneous symmetry breaking in the moiré pattern. At $\nu = 1$, holes are located at corners of the honeycomb and leave the adjacent sites empty, which breaks C_6 symmetry to C_3 and minimizes Coulomb interactions. This broken C_6 symmetry will then get restored if doping one more hole. All moiré potential minima will be occupied by holes and make a perfect honeycomb lattice. As the doping increases to $\nu = 3$, two spin-opposite holes are forced to accompany each other in one corner of the honeycomb despite the Coulomb repulsion, forming a more diffuse pattern than the adjacent singly occupied site. This leads to two distinct density patterns appearing in the sites of the honeycomb, breaking the C_6 symmetry to C_3 , and the symmetry will again get restored at $\nu = 4$ since all the sites are doubly occupied then. At $\nu = 5$, a special density pattern appears, which exhibits a mirror symmetry. It is also worth noting that (5, 3/2) state are nearly degenerate with the calculated ground state (5, 1/2) while showing a distinct

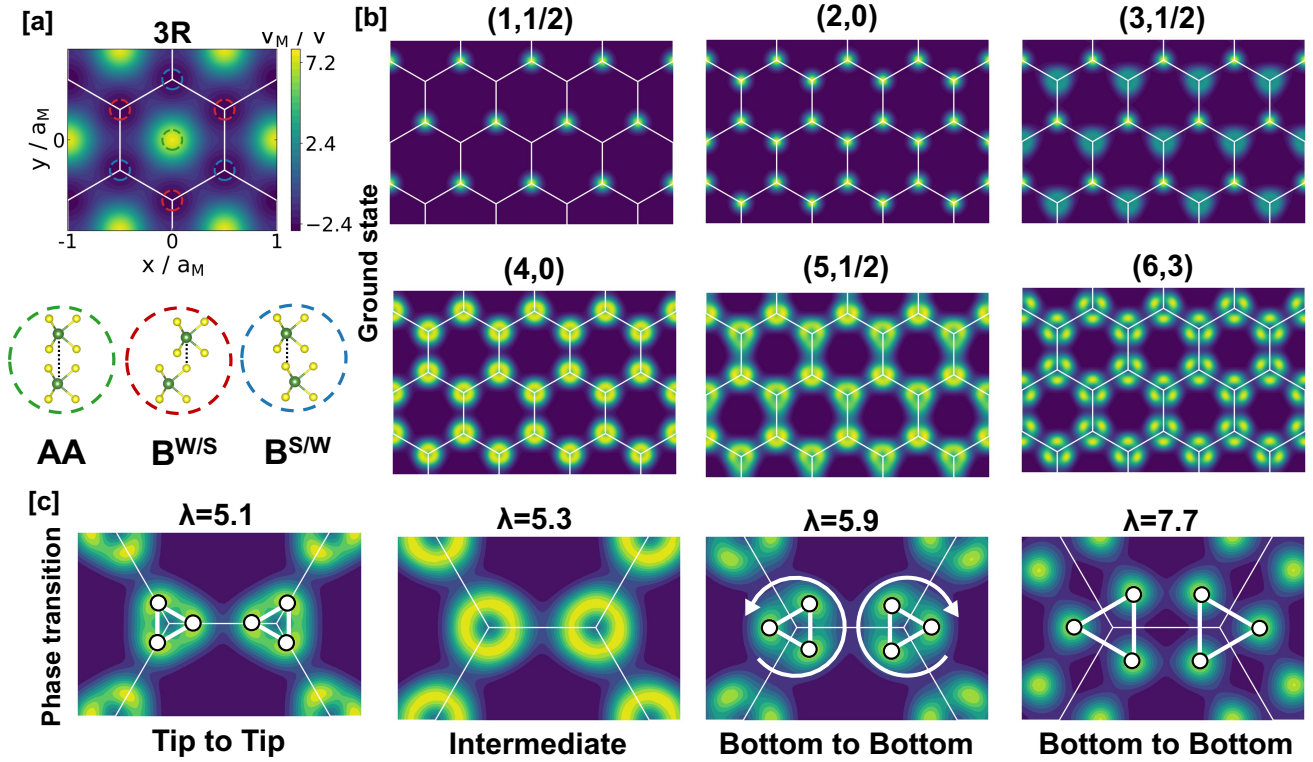


Fig. 3 | Calculated density pattern of 3R WS₂ homobilayer. Tuples above the figure denote the particle fillings and the magnetic number of spin (ν , S_z). **a**, moiré potential of 3R WS₂ homobilayer. a_M denotes length of moiré cell and is set to 16.51 nm. **b**, calculated ground states at different particle fillings ν . **c**, phase transition of (6, 3) state at different interaction ratio λ . λ measures the strength ratio between Coulomb repulsion and moiré potential attraction. Moiré potential amplitude V is tuned to control λ . The orientation of trimers get flipped with increasing λ to avoid strong Coulomb repulsion.

C_3 symmetry in Supplementary Figs. 3 and 4.

When the filling ν reaches 6, trimers form in the sites of the honeycomb lattice. The trimers have different orientations and an intriguing phase transition can be induced by tuning either the Coulomb repulsion or the moiré potential attraction. In Fig. 3c, we plot the zoom-in pattern of the (6, 3) state at varying interactions, defined by the interaction ratio $\lambda \sim \epsilon^{-1} V^{-1/4}$ [12]. When the moiré potential attraction dominates over the Coulomb repulsion, these two triangles get placed in a tip-to-tip manner, which resembles the shape of moiré potential. As the Coulomb repulsion gets stronger, triangles become larger and gradually melt into circles, finally getting flipped and forming a bottom-to-bottom pattern. Holes are then placed in the saddle points of moiré potential, which avoids strong Coulomb interaction compared to the tip-to-tip pattern.

Wigner covalent crystal Up to now, most discovered Wigner phases appear as atomic crystals and molecular crystals, where “atoms” or “molecules” are isolated units that resemble chemical atoms and molecules. Interestingly, the equivalent of bonding commonly seen in molecules is notably absent in studies of Wigner phases. Here, by tuning the filling number and spin polarization, we show that it is possible to form covalent bonding in moiré systems. Fig. 4a shows a schematic plot of the formation mechanism of a covalent bond between two Wigner molecules. Assuming each molecule already has several holes forming a relatively stable state, then excess holes would feel repulsive inter-

actions from the existing holes. They will be pushed towards the middle regime of two molecules and reach equilibrium. This mechanism is similar to the “sharing” of electrons between two covalent bonded molecules. Such a mechanism can be further facilitated by enhancing Pauli exclusion, which is achievable by applying a magnetic field to align the spin of all holes in the same orientation (Fig. 4a).

Fig. 4b demonstrates the emergence of covalent bonds in fully polarized Wigner phases. Specifically, the first panel shows the formation of covalent bonds in a fully polarized $\nu = 3$ state when an additional hole is doped into the C_6 symmetric $\nu = 2$ state. Consequently, the honeycomb lattice of the $\nu = 2$ state deforms due to Coulomb interactions, breaking its C_6 symmetry down to C_2 . Similar situations occur in polarized $\nu = 5$ and 7 states, except that the honeycomb sites are now occupied by dimers and trimers respectively. As we further increase the filling to $\nu = 9$, honeycomb sites are connected in a network of covalent bonds, forming a novel crystal, which we dub “Wigner covalent crystal” following the existing names of Wigner crystal and Wigner molecular crystal. The Wigner covalent phase adds another key member to the family of Wigner phases.

Discussion Moiré materials host various novel phenomena, tightly related to strong correlations. Despite the rapid development of experimental observation, the simulation approach of these materials remains at an early stage, which hinders a thorough understanding of the strongly correlated phenomena. In this

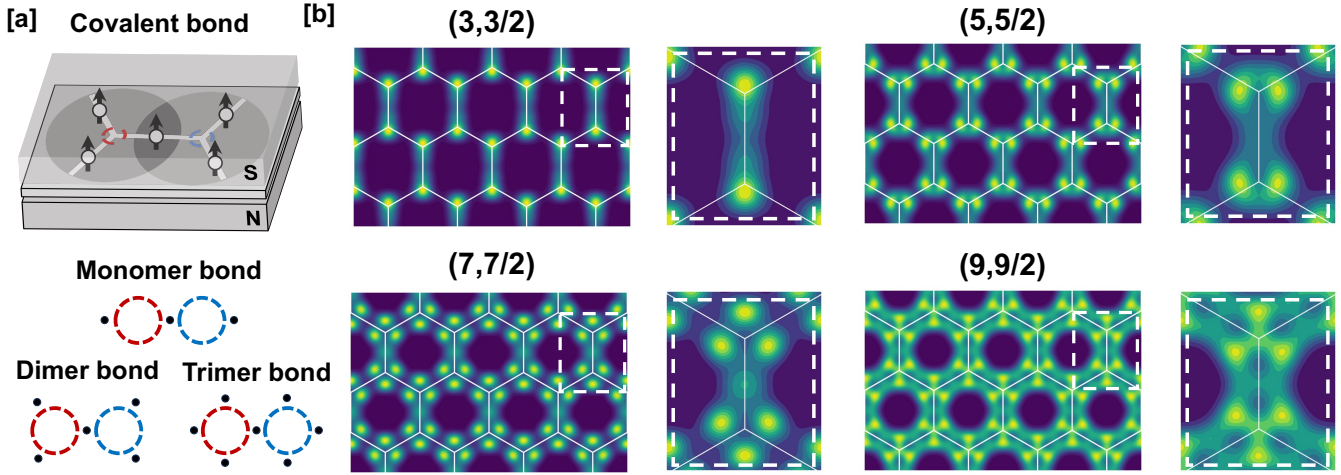


Fig. 4 | Calculated covalent states of 3R WS₂ homobilayer. **a**, schematic plot of covalent bond formation in Wigner phases. Upper panel: formation of covalent bond in a spin polarized system. Lower panel: particle patterns of the monomer, dimer and trimer bond. Colored circles denote B^{W/S} and B^{S/W} regions of 3R WS₂ respectively. **b**, particle density pattern of several calculated covalent states. a_M is set to 16.51 nm. Tuples above the figure denote the particle fillings and the magnetic number of spin (ν, S_z). In each sub-panel, the right figure shows a zoom-in of the covalent bond.

work, we described a deep learning approach to simulate moiré materials with a rigorous treatment of electron correlations. Our simulations reveal numerous exotic phases with varying symmetries, demonstrating the generality, accuracy, and efficiency of this approach for exploring moiré materials. Besides providing novel moiré patterns, our framework can also be extended to predict more material behaviors and properties, bypassing certain experimental constraints. This work will help accelerate the discovery of new moiré materials, including multi-layer systems, and their applications in the future. Furthermore, our approach shows promise for broader research areas, such as the quantum transparency phenomenon and the anomalous Hall effect.

Methods

Effective model of TMD Moiré materials are known to contain enormous atom numbers in the unit cell, which pose a great challenge for direct *ab initio* simulations. Nonetheless, an effective model can be derived for doping holes in TMD materials to simplify the problem [4, 24].

According to the density functional theory (DFT) result [4, 24], heterobilayers such as WSe₂/WS₂ exhibit valence band maximums located at K and K' points of the Brillouin zone, which have the same energy but opposite spin due to spin-orbit coupling. On the other hand, homobilayers such as WS₂ show valence band maximums located at Γ point with spin degeneracy, as a result of Kramers' theorem. In either case, the most active valence states show a spin degeneracy, which can be treated as a quasi-particle with spin degrees as shown in Eq. (2). Furthermore, the effective mass m^* is fitted to describe the dispersion of DFT valence band edge and moiré potential is derived to mimic the interaction between doping holes and inertia electrons far below Fermi surface, see Refs. [4, 24, 30] for more detailed derivations. When the moiré system gets twisted to critical angles, flat bands appear indicating that the effective mass of the particle approaches infinity. Kinetic energy vanishes and Coulomb interaction dominates in the Hamiltonian, which requires high-accuracy wavefunction

methods to incorporate correlations among particles.

It's also worth noting that the moiré potential of 3R materials shows a slightly different form from Eq. (2) [24], which reads

$$\begin{aligned}
 V_M^{3R}(\mathbf{r}) &= -2 \sum_{i=1}^3 \sum_{s=1}^3 V_s \cos(\mathbf{b}_i^s \cdot \mathbf{r} + \phi), \\
 \mathbf{b}_i^1 &= \frac{4\pi}{\sqrt{3}a_M} \left(\sin \frac{2\pi i}{3}, \cos \frac{2\pi i}{3} \right), \\
 \mathbf{b}_i^2 &= \frac{4\pi}{a_M} \left[\sin \left(\frac{2\pi i}{3} + \frac{\pi}{6} \right), \cos \left(\frac{2\pi i}{3} + \frac{\pi}{6} \right) \right], \\
 \mathbf{b}_i^3 &= \frac{8\pi}{\sqrt{3}a_M} \left(\sin \frac{2\pi i}{3}, \cos \frac{2\pi i}{3} \right),
 \end{aligned} \tag{3}$$

where \mathbf{b}_i^s denote reciprocal vectors of different shells. Specific parameters of various materials are summarized in Supplementary Note 2.

Neural network architecture Our neural network resembles similar architecture to previously proposed networks for solid materials and uniform electron gas [20, 22].

Particle features \mathbf{r}_i are combined with each other and form permutation equivalent features \mathbf{f}_i [18]

$$\begin{aligned}
 \mathbf{f}_i &= \text{concat} \left[\mathbf{g}_i^S, \mathbf{g}_i^D \right], \\
 \mathbf{g}_i^S &= \text{concat} \left[\sin(\mathbf{r}_i \cdot \mathbf{b}), \sum_j \sin(\mathbf{r}_j \cdot \mathbf{b}) \mathbf{a} \right], \\
 \mathbf{g}_i^D &= \text{concat} \left[\sum_j \sin[(\mathbf{r}_i - \mathbf{r}_j) \cdot \mathbf{b}] \mathbf{a}, \sum_j d(\mathbf{r}_i - \mathbf{r}_j) \right].
 \end{aligned}$$

These features are subsequently fed into a neural network to construct effective orbital functions $u_{\mathbf{k}_i}$ which capture correlations between particles

$$u_{\mathbf{k}_i}(\mathbf{r}_1, \dots, \mathbf{r}_N) = \text{Network}(\mathbf{f}_j).$$

These orbitals are then combined with a momentum dependent phase factor $e^{ik_i \cdot \mathbf{r}_j}$ to become elements of Slater determinants, which forms a legal antisymmetric many-body wavefunction for particles in moiré superlattice. To ensure the periodic boundary condition, we employ the triangle distance input feature $d(\mathbf{r})$, which reads [22]

$$4\pi^2 d^2(\mathbf{r}) = \sum_{ij} \sin(\mathbf{r} \cdot \mathbf{b}_i) \sin(\mathbf{r} \cdot \mathbf{b}_j) \mathbf{a}_i \cdot \mathbf{a}_j + [1 - \cos(\mathbf{r} \cdot \mathbf{b}_i)][1 - \cos(\mathbf{r} \cdot \mathbf{b}_j)] \mathbf{a}_i \cdot \mathbf{a}_j. \quad (4)$$

Specific hyperparameters of network are given in Supplementary Note 1.

Neural network optimization Considering the wide range of length scale in moiré superlattice, we rescale the effective model $\mathbf{r} \rightarrow a_M \mathbf{r}'$ for computational convenience, which reads

$$\hat{H}' \equiv \sum_i \left[-\frac{\Delta'_i}{2} + m^* a_M^2 V_M(\mathbf{r}'_i) \right] + \frac{1}{2} \sum_{i \neq j} \frac{m^* a_M}{\epsilon |\mathbf{r}'_i - \mathbf{r}'_j|}. \quad (5)$$

Our networks is optimized to minimize the scaled Hamiltonian \hat{H}' , whose gradient reads

$$\nabla \langle E_l \rangle = 2 \operatorname{Re} \left[\langle E_l \nabla \ln \Psi^* \rangle - \langle E_l \rangle \langle \nabla \ln \Psi^* \rangle \right], \quad (6)$$

$$E_l = \Psi^{-1} \hat{H}' \Psi,$$

and $\langle \dots \rangle$ denotes the expectations of operators with $|\Psi|^2$ distribution. Moreover, Kronecker factored curvature estimator (KFAC) optimizer [31] is employed to train the neural network towards the ground states at different fillings and spin polarization.

Moiré pattern analysis To visualize the Wigner phases, we plot the particle density $\rho(\mathbf{r})$ derived from many-body wavefunction Ψ

$$\rho(\mathbf{r}) = N \int d^3 \mathbf{r}_2 \cdots d^3 \mathbf{r}_N |\Psi(\mathbf{r}, \mathbf{r}_2, \dots, \mathbf{r}_N)|^2. \quad (7)$$

In practice, ρ is evaluated by accumulating Monte Carlo samples of particles on a 100×100 uniform grid over the moiré cell.

Workflow and computational details Supercell approximation is employed in our simulations. Particles are initialized uniformly in the moiré supercell, and gradually form moiré patterns during energy minimization. The expectations of operators are evaluated via the Monte Carlo approach. Forward Laplacian technique is employed to speed up the simulation [32]. Most simulations in this work are performed on eight A800 graphics processing units within several hours. Training curves of each system are plotted in Supplementary Figs. 1-3. Other excited states are plotted in Supplementary Fig. 5. Calculated energy and geometry are listed in Supplementary Note 3.

Data availability

The data generated in this study are provided in the Supplementary Information.

Code availability

This work is developed upon open-source DeepSolid [33] on GitHub.

References

- [1] Rafi Bistritzer and Allan H MacDonald. Moiré bands in twisted double-layer graphene. *Proceedings of the National Academy of Sciences*, 108(30):12233–12237, 2011.
- [2] Yuan Cao, Valla Fatemi, Shiang Fang, Kenji Watanabe, Takashi Taniguchi, Efthimios Kaxiras, and Pablo Jarillo-Herrero. Unconventional superconductivity in magic-angle graphene superlattices. *Nature*, 556(7699):43–50, 2018.
- [3] Yuan Cao, Valla Fatemi, Ahmet Demir, Shiang Fang, Spencer L Tomarken, Jason Y Luo, Javier D Sanchez-Yamagishi, Kenji Watanabe, Takashi Taniguchi, Efthimios Kaxiras, et al. Correlated insulator behaviour at half-filling in magic-angle graphene superlattices. *Nature*, 556(7699):80–84, 2018.
- [4] Fengcheng Wu, Timothy Lovorn, Emanuel Tutuc, and A. H. MacDonald. Hubbard model physics in transition metal dichalcogenide moiré bands. *Phys. Rev. Lett.*, 121:026402, Jul 2018.
- [5] Yanhao Tang, Lizhong Li, Tingxin Li, Yang Xu, Song Liu, Katayun Barkmak, Kenji Watanabe, Takashi Taniguchi, Allan H. MacDonald, Jie Shan, and Kin Fai Mak. Simulation of hubbard model physics in wse2/ws2 moiré-superlattices. *Nature*, 579(7799):353–358, 2020.
- [6] Yang Xu, Song Liu, Daniel A. Rhodes, Kenji Watanabe, Takashi Taniguchi, James Hone, Veit Elser, Kin Fai Mak, and Jie Shan. Correlated insulating states at fractional fillings of moiré-superlattices. *Nature*, 587(7833):214–218, 2020.
- [7] Hongyuan Li, Shaowei Li, Emma C. Regan, Danqing Wang, Wenyu Zhao, Salman Kahn, Kentaro Yumigeta, Mark Blei, Takashi Taniguchi, Kenji Watanabe, Sefaattin Tongay, Alex Zettl, Michael F. Crommie, and Feng Wang. Imaging two-dimensional generalized wigner crystals. *Nature*, 597(7878):650–654, 2021.
- [8] Emma C. Regan, Danqing Wang, Chenhao Jin, M. Iqbal Bakti Utama, Beini Gao, Xin Wei, Sihang Zhao, Wenyu Zhao, Zuocheng Zhang, Kentaro Yumigeta, Mark Blei, Johan D. Carlström, Kenji Watanabe, Takashi Taniguchi, Sefaattin Tongay, Michael Crommie, Alex Zettl, and Feng Wang. Mott and generalized wigner crystal states in wse2/ws2 moiré-superlattices. *Nature*, 579(7799):359–363, 2020.
- [9] Xiong Huang, Tianmeng Wang, Shengnan Miao, Chong Wang, Zhipeng Li, Zhen Lian, Takashi Taniguchi, Kenji Watanabe, Satoshi Okamoto, Di Xiao, Su-Fei Shi, and Yong-Tao Cui. Correlated insulating states at fractional fillings of the ws2/wse2 moiré-lattice. *Nature Physics*, 17(6):715–719, 2021.
- [10] Eva Y Andrei, Dmitri K Efetov, Pablo Jarillo-Herrero, Allan H MacDonald, Kin Fai Mak, T Senthil, Emanuel Tutuc, Ali Yazdani, and Andrea F Young. The marvels of moiré materials. *Nature Reviews Materials*, 6(3):201–206, 2021.
- [11] Fengcheng Wu, A. H. MacDonald, and Ivar Martin. Theory of phonon-mediated superconductivity in twisted bilayer graphene. *Phys. Rev. Lett.*, 121:257001, Dec 2018.
- [12] Aidan P. Reddy, Trithip Devakul, and Liang Fu. Artificial atoms, wigner molecules, and an emergent kagome lattice in semiconductor moiré superlattices. *Phys. Rev. Lett.*, 131:246501, Dec 2023.
- [13] Hongyuan Li, Ziyu Xiang, Aidan P Reddy, Trithip Devakul, Renee Sailus, Rounak Banerjee, Takashi Taniguchi, Kenji Watanabe, Sefaattin Tongay, Alex Zettl, et al. Wigner molecular crystals from multi-electron moiré artificial atoms. *arXiv preprint arXiv:2312.07607*, 2023.
- [14] Shu Fay Ung, Joonho Lee, and David R Reichman. Competing generalized wigner crystal states in moiré heterostructures. *Physical Review B*, 108(24):245113, 2023.
- [15] Yubo Yang, Miguel A. Morales, and Shiwei Zhang. Metal-insulator transition in a semiconductor heterobilayer model. *Phys. Rev. Lett.*, 132:076503, Feb 2024.
- [16] Giuseppe Carleo and Matthias Troyer. Solving the quantum many-body problem with artificial neural networks. *Science*, 355(6325):602–606, 2017.
- [17] Jiequn Han, Linfeng Zhang, and Weinan E. Solving many-electron schrödinger equation using deep neural networks. *Journal of Computational Physics*, 399:108929, 2019.
- [18] David Pfau, James S. Spencer, Alexander G. D. G. Matthews, and W. M. C. Foulkes. Ab initio solution of the many-electron schrödinger equation with deep neural networks. *Phys. Rev. Res.*, 2:033429, Sep 2020.

- [19] Jan Hermann, Zeno Schätzle, and Frank Noé. Deep-neural-network solution of the electronic schrödinger equation. *Nature Chemistry*, 12(10):891–897, 2020.
- [20] Xiang Li, Zhe Li, and Ji Chen. Ab initio calculation of real solids via neural network ansatz. *Nature Communications*, 13(1):7895, 2022.
- [21] Max Wilson, Saverio Moroni, Markus Holzmann, Nicholas Gao, Filip Wudarski, Tejs Vegge, and Arghya Bhowmik. Neural network ansatz for periodic wave functions and the homogeneous electron gas. *Phys. Rev. B*, 107:235139, Jun 2023.
- [22] Gino Cassella, Halvard Sutterud, Sam Azadi, ND Drummond, David Pfau, and James S Spencer. Discovering quantum phase transitions with fermionic neural networks. *Physical Review Letters*, 130(3):036401, 2023.
- [23] Di Luo, Aidan P Reddy, Trithep Devakul, and Liang Fu. Artificial intelligence for artificial materials: moiré atom. *arXiv preprint arXiv:2303.08162*, 2023.
- [24] Mattia Angeli and Allan H MacDonald. γ valley transition metal dichalcogenide moiré bands. *Proceedings of the National Academy of Sciences*, 118(10):e2021826118, 2021.
- [25] Constantine Yannouleas and Uzi Landman. Wigner-molecule supercrystal in transition metal dichalcogenide moiré superlattices: Lessons from the bottom-up approach. *Physical Review B*, 109(12):L121302, 2024.
- [26] Constantine Yannouleas and Uzi Landman. Quantum wigner molecules in moiré materials. *Phys. Rev. B*, 108:L121411, Sep 2023.
- [27] Shu Fay Ung, Joonho Lee, and David R. Reichman. Competing generalized wigner crystal states in moiré heterostructures. *Phys. Rev. B*, 108:245113, Dec 2023.
- [28] Chenhao Jin, Zui Tao, Tingxin Li, Yang Xu, Yanhao Tang, Jiacheng Zhu, Song Liu, Kenji Watanabe, Takashi Taniguchi, James C Hone, et al. Stripe phases in wse₂/ws₂ moiré superlattices. *Nature Materials*, 20(7):940–944, 2021.
- [29] Yang Zhang, Noah FQ Yuan, and Liang Fu. Moiré quantum chemistry: charge transfer in transition metal dichalcogenide superlattices. *Physical Review B*, 102(20):201115, 2020.
- [30] Jeil Jung, Arnaud Raoux, Zhenhua Qiao, and A. H. MacDonald. Ab initio theory of moiré superlattice bands in layered two-dimensional materials. *Phys. Rev. B*, 89:205414, May 2014.
- [31] James Martens and Roger Grosse. Optimizing neural networks with kronecker-factored approximate curvature. In *International conference on machine learning*, pages 2408–2417. PMLR, 2015.
- [32] Ruichen Li, Haotian Ye, Du Jiang, Xuelan Wen, Chuwei Wang, Zhe Li, Xiang Li, Di He, Ji Chen, Weiluo Ren, and Liwei Wang. A computational framework for neural network-based variational Monte Carlo with Forward Laplacian. *Nature Machine Intelligence*, 6(2):209–219, February 2024.
- [33] Xiang Li. bytedance/deepsolid: Release 1.0, December 2022.

Acknowledgements

We want to thank Hongyuan Li for discussion. We want to thank ByteDance Research Group for inspiration and encouragement. This work is directed and supported by Hang Li and ByteDance Research. This work is supported by the National Key R&D Program of China (2021YFA1400500 to J.C., 2021YFA1401300 to Y.X.) and the Strategic Priority Research Program of Chinese Academy of Sciences (XDB33000000).

Author contributions

X.L., Y.X. and J.C. conceived the study; X.L. developed the method, performed implementations, simulations and data analysis; Y.X. and J.C. supervised the project. X.L., Y.Q., W.R., Y.X., and J.C. wrote the paper.

Supplementary information: Emergent Wigner phases in moiré superlattice from deep learning

Xiang Li et al

Supplementary Note 1. Hyperparameters for simulations

The recommended hyperparameters are listed in Supplementary Table 1.

Supplementary Table 1 | Recommended hyperparameters

Hyperparameter	Value	Hyperparameter	Value
Dimension of one electron layer \mathbf{V}	256	Dimension of two electron layer \mathbf{W}	32
Number of layers	4	Number of determinants	8
Optimizer	KFAC	Learning rate	1e-2
Damping	1e-3	Constrained norm of gradient	1e-3
Momentum of optimizer	0.0	Batch size	4096
Number of training steps	5e4	Clipping window of gradient	5
MCMC burn in	1e3	MCMC steps between each iterations	30
MCMC move width	2e-2	Target MCMC acceptance	55%
Precision	Float32	Number of inference steps	1e4

Supplementary Note 2. Parameter of moiré potential

Employed model parameters of WSe_2/WS_2 and 2H WS_2 are taken from Refs. [1, 2] and listed in Supplementary Table 2.

Supplementary Table 2 | Model parameters of WSe_2/WS_2 and 2H WS_2 .

Systems	V / meV	m^*/m_e	ϕ	ϵ
WSe_2/WS_2	15	0.5	45°	5
2H WS_2	10.3	0.9	20°	5

Model of 3R WS_2 has a slightly different form and its parameters are listed in Supplementary Table 3 [3].

Supplementary Table 3 | Model parameters of 3R WS_2

Systems	V_1 / meV	V_2 / meV	V_3 / meV	m^*/m_e	ϕ	ϵ
3R WS_2	33.5	4.0	5.5	0.87	180°	5

Supplementary Note 3. Calculated energy and geometry

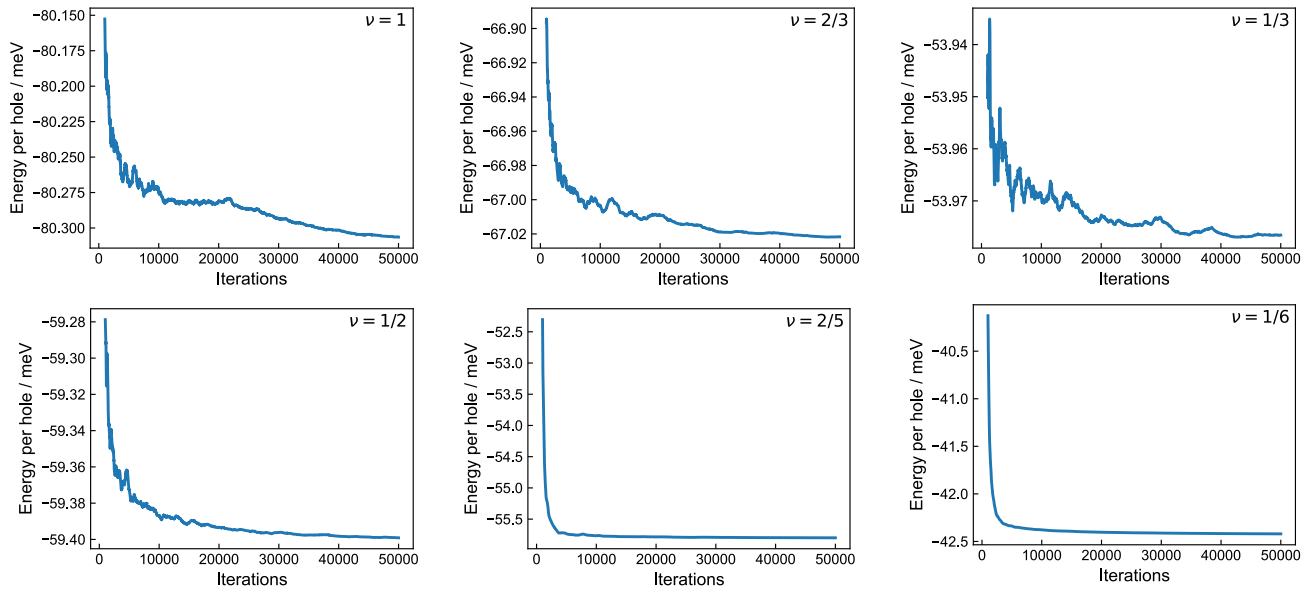
Calculated energies and geometry of each system are listed in Supplementary Table 4.

Supplementary Table 4 | Calculated energies and geometry of each system

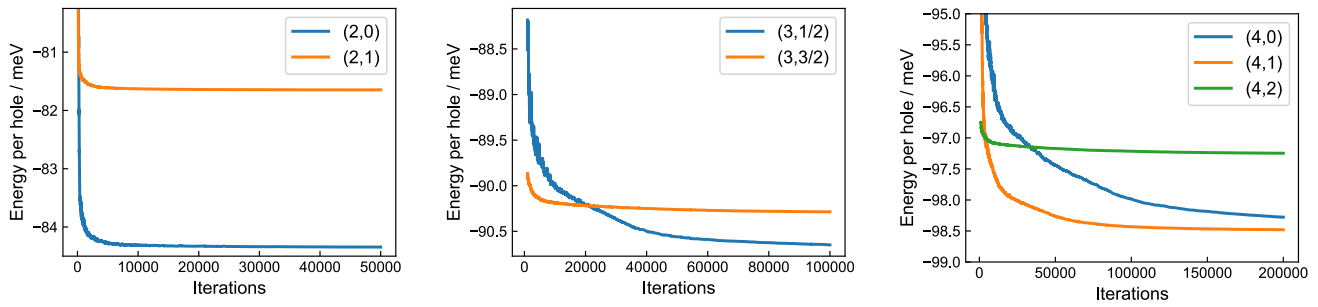
Systems	a_M / nm	fillings ν	S_z	energy per hole / meV	lattice vectors / a_M	supercell size
WSe ₂ /WS ₂	8.3	1	1	-80.2965(2)	$a_1 = (1, 0), a_2 = (1/2, \sqrt{3}/2)$	5 × 5
		2/3	1	-67.0221(1)	$a_1 = (3/2, \sqrt{3}/2), a_2 = (-3/2, \sqrt{3}/2)$	4 × 4
		1/3	1/2	-53.97697(9)	$a_1 = (1, 0), a_2 = (1/2, \sqrt{3}/2)$	5 × 5
		1/2	1	-59.39885(9)	$a_1 = (2, 0), a_2 = (1, \sqrt{3})$	4 × 4
		2/5	5	-55.7933(2)	$a_1 = (5, 0), a_2 = (5/2, 5\sqrt{3}/2)$	2 × 2
		1/6	3	-42.41933(9)	$a_1 = (6, 0), a_2 = (3, 3\sqrt{3})$	2 × 2
2H WS ₂	9.8	2	0	-84.3421(2)	$a_1 = (1, 0), a_2 = (1/2, \sqrt{3}/2)$	3 × 3
		2	1	-81.64466(7)		
2H WS ₂	9.8	3	1/2	-90.6866(2)	$a_1 = (1, 0), a_2 = (1/2, \sqrt{3}/2)$	4 × 4
		3	3/2	-90.2980(1)		
2H WS ₂	9.8	4	0	-98.2843(3)	$a_1 = (1, 0), a_2 = (1/2, \sqrt{3}/2)$	4 × 4
		4	1	-98.4657(2)		
		4	2	-97.2430(1)		
3R WS ₂	16.51	1	1/2	-102.51681(7)	$a_1 = (1, 0), a_2 = (1/2, \sqrt{3}/2)$	3 × 3
		2	1	-114.6824(2)		
		6	3	-110.5943(2)		
		7	7/2	-110.9851(1)		
		9	9/2	-113.4288(2)		
3R WS ₂	16.51	3	1/2	-109.0860(1)	$a_1 = (1, 0), a_2 = (1/2, \sqrt{3}/2)$	3 × 3
		3	3/2	-107.58514(8)		
		4	0	-110.2786(2)		
		4	1	-108.8960(1)		
		4	2	-107.8524(1)		
		5	1/2	-109.5465(1)		
		5	3/2	-109.54138(9)		
		5	5/2	-108.56062(6)		

Supplementary Note 4. Training curves

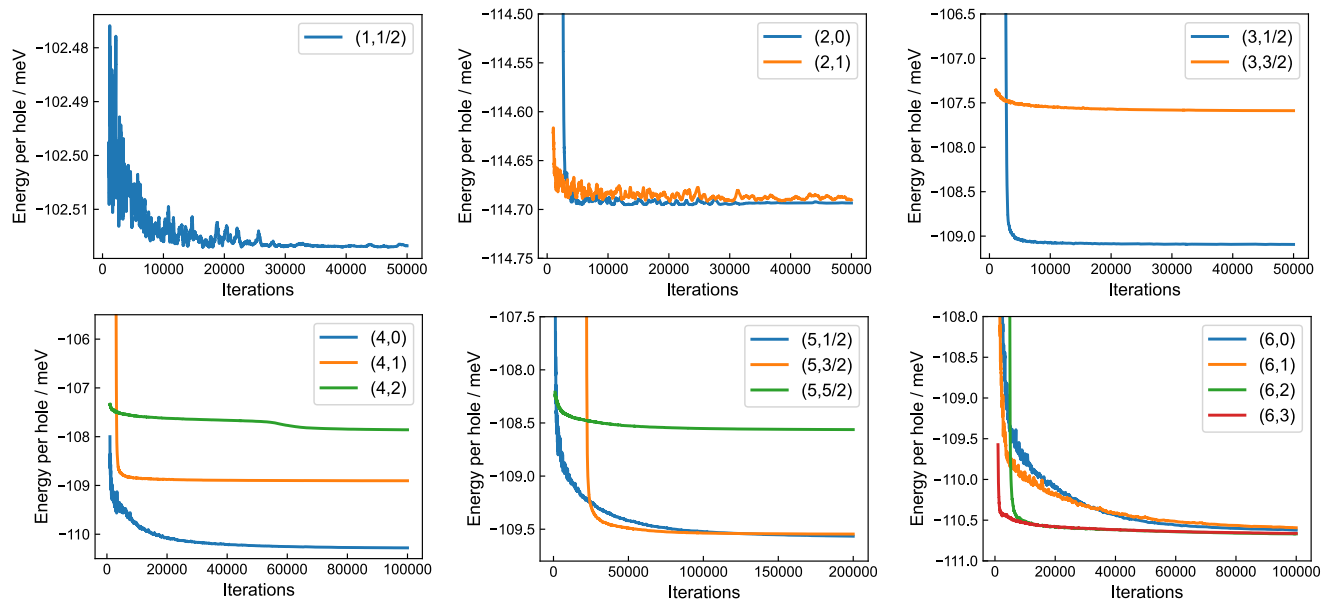
Training curves of each system are plotted in Supplementary Figs. 1 to 3.



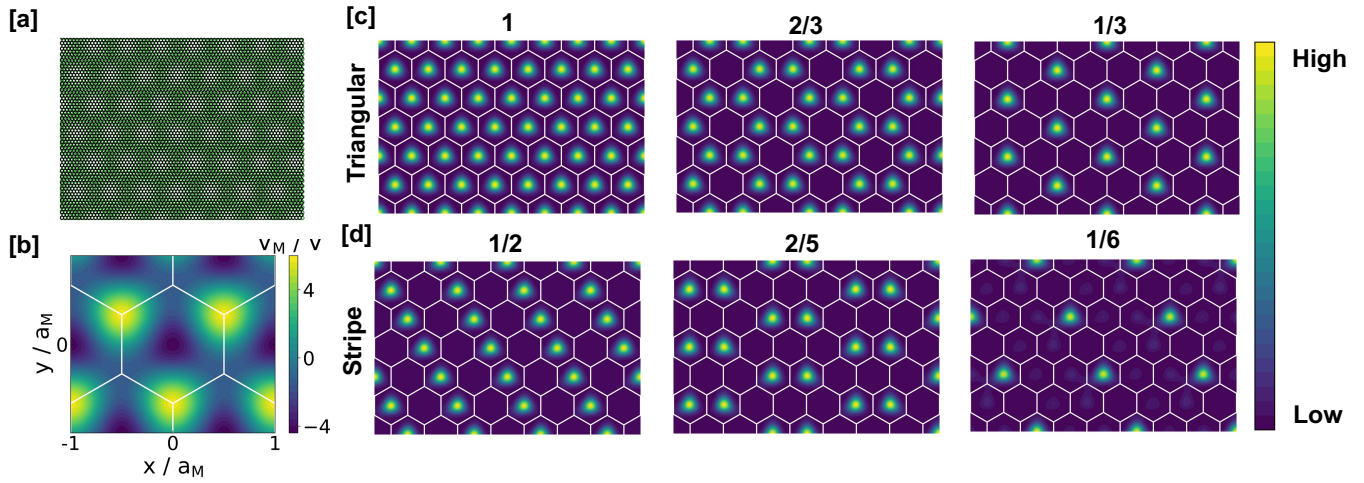
Supplementary Figure 1 | Training curve of various states in WSe_2/WS_2 .



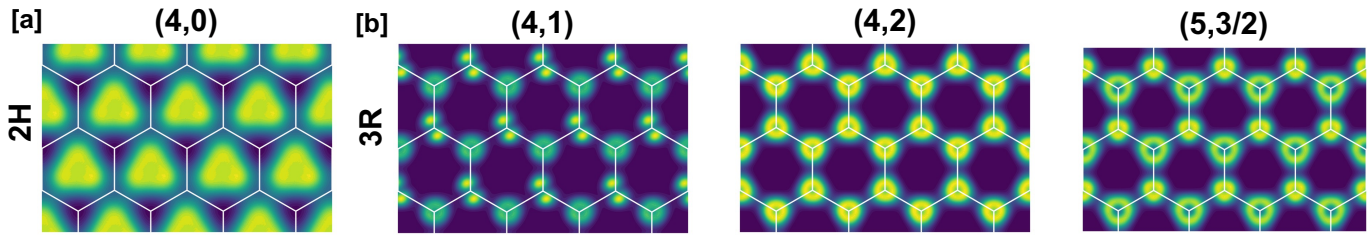
Supplementary Figure 2 | Training curve of various states in $2H WS_2$. Tuples in the legends denote the particle fillings and the magnetic number of spin (ν, S_z).



Supplementary Figure 3 | Training curve of various states in $3R WS_2$. Tuples in the legends denote the particle fillings and the magnetic number of spin (ν, S_z).



Supplementary Figure 4 | Calculated hole density pattern of WSe_2/WS_2 heterobilayer. Numbers above the figures denote the particle fillings ν . **a**, structure of the WSe_2/WS_2 superlattice. **b**, moiré potential of WSe_2/WS_2 . a_M denotes corresponding length of moiré cell and is set to 8.3 nm. **c**, calculated triangular phase at fillings $\nu = 1, 2/3, 1/3$. **d**, calculated stripe phase at fillings $\nu = 1/2, 2/5, 1/6$.



Supplementary Figure 5 | Other density patterns of the WS_2 system. Tuples above the figure denote the particle fillings and the spin quantum number (ν, S_z) . **a-b**, moiré pattern of 2H and 3R WS_2 respectively. All other states with $\nu = 2$ and 6 of the 3R WS_2 system show the same moiré pattern regardless of S_z .

Supplementary Note 5. Other states

Generalized Wigner crystal states and other excited states are plotted in Figs. 4 and 5.

Supplementary References

- [1] Hongyuan Li, Ziyu Xiang, Aidan P Reddy, Trithep Devakul, Renee Sailus, Rounak Banerjee, Takashi Taniguchi, Kenji Watanabe, Sefaattin Tongay, Alex Zettl, et al. Wigner molecular crystals from multi-electron moiré' artificial atoms. *arXiv preprint arXiv:2312.07607*, 2023.
- [2] Yang Zhang, Noah FQ Yuan, and Liang Fu. Moiré quantum chemistry: charge transfer in transition metal dichalcogenide superlattices. *Physical Review B*, 102(20):201115, 2020.
- [3] Mattia Angeli and Allan H MacDonald. γ valley transition metal dichalcogenide moiré bands. *Proceedings of the National Academy of Sciences*, 118(10):e2021826118, 2021.